Improving Proton Conductivity by Navigating Proton Trapping in High Scandium-Doped Barium Zirconate Electrolytes

Clarita Y. Regalado Vera, Hanping Ding,* Jagoda Urban-Klaehn, Meng Li, Zeyu Zhao, Frederick Stewart, Hanchen Tian, Xingbo Liu, Yanhao Dong, Ju Li, Meng Zhou, Hongmei Luo,* and Dong Ding*

Read Online

ACCESS | Metrics & More | Article Recommendations | Supporting Information

ABSTRACT: Proton-conducting oxides are used in intermediate-temperature (300 °C < T < 700 °C) applications of fuel cells, electrolyzers, membrane reactors, hydrogen pumps, and sensors. The proton conductivity of doped ABO_3 perovskites is partly dependent on the proton concentration and hence on the level of material hydration. However, how the material hydration ability is affected by differences in doping is not fully understood. Here, we show the prospect of proton trapping and detrapping that influences material hydration and dehydration. The proton-trapping influence is significant for Sc-doped $BaZrO_3$ compared to Y-doped $BaZrO_3$. Our work offers a perspective to understand how defect interaction/associations influence the hydration ability of proton-conducting oxides. Furthermore, positron annihilation lifetime spectroscopy was revealed to be a valuable technique for studying the proton-trapping phenomena and the defect chemistry of dense proton conductors. Density functional theory calculations also showed that a high hydration level in Sc-doped $BaZrO_3$ boosts proton migration. In contrast, the effect of boosting the proton migration due to increased hydration is limited for Y-doped $BaZrO_3$. This effect, in turn, might explain the trend of conductivity with dopant concentration in doped $BaZrO_3$.
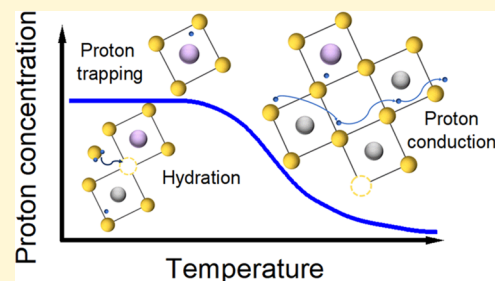
INTRODUCTION

Proton-conducting perovskite ceramics with an ABO_3 structure are applied in fuel cells, electrolyzers, membrane reactors, hydrogen separation membranes, and hydrogen sensors.[1−5] Among the available solid oxide proton conductors, barium zirconate ($BaZrO_3$) perovskite is one of the leading candidates for large-scale application, mainly due to its chemical stability in a steam environment and high proton conductivity. Maximizing the $BaZrO_3$ proton conductivity has been accomplished through addition of dopants at optimized levels.[6−8] Typically for proton-conducting perovskite-type electrolytes, the protons, $OH_o^•$, are formed by the hydration of an oxygen vacancy, $V_o^{••}$, which is favored at lower temperatures

$$H_2O + V_O^{••} + O_O^× \leftrightarrow 2OH_O^• \qquad (1)$$
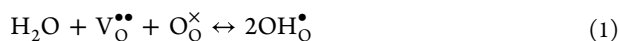
Proton conductivity is proportionally limited by the oxygen vacancy concentration and degree of hydration. To create oxygen vacancies, the Zr sites are doped with trivalent elements.[7,9] Oxygen vacancies are generated to compensate for charge neutrality. Using doping levels that keep the lattice structure stable, and by ensuring all oxygen vacancies are hydrated both serve to maximize the proton concentration. However, there is a limitation to oxygen vacancy hydration due to high energies associated with their hydration and its dependence on the lattice structure, environment, and defect associations.[10−17] With Y-doped $BaZrO_3$, the ideal level is 20

mol %, $BaZr_{0.8}Y_{0.2}O_{3−δ}$ (BZY20), where it reaches the highest conductivity taking into account the optimum compromise between high hydration level and structure stability.[6,7,18,19]

Fundamentally, the limit on material hydration is closely related to complicated proton processes within the lattice, Figure 1. When protons migrate via reorientation and jump between two oxygen atoms,[13,20] they may experience attraction from dopant atoms, known as proton trapping, resulting in reduced proton mobility.[21,22] The proton-trapping effect is more severe at lower temperatures and higher doping levels.[14,18] Therefore, proton conduction as a function of temperature might be influenced by hydration and proton-trapping processes, which in turn can be a function of the dopant type and concentration. For instance, when the temperature increases, a proton experiencing trapping might exit the material by dehydration, remain in the proton trap, or migrate to a nonproton-trapping position (Figure 1a). For the proton that migrates to a nonproton-trapping position, an increase in temperature can result in its removal by dehydration. Similarly, when the temperature decreases, a
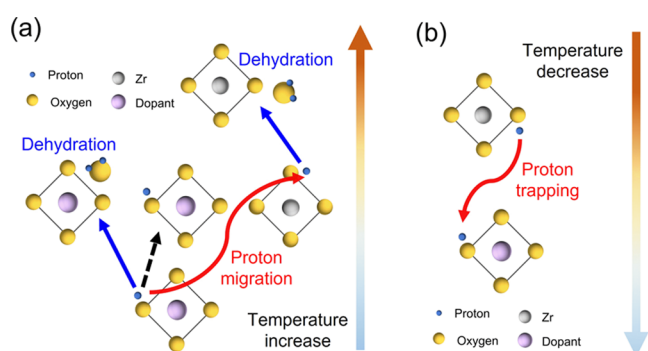
Figure 1. Possible proton processes in doped BaZrO$_3$ as a function of temperature: (a) for a trapped proton when the temperature is increased and (b) for a trap-free proton when the temperature is decreased.

proton in a nonproton-trapping position might migrate to a trap (Figure 1b).

While BZY20 is currently considered the benchmark composition for BaZrO$_3$-based materials, past studies have shown (1) reduced proton concentrations at temperatures higher than 500 °C,[6] (2) electronic conduction in oxidizing atmospheres,[23] (3) Y-segregation at the surface of densified samples,[24] and (4) Y-segregation at the space charge region along grain boundaries.[25] Any of these could negatively affect its performance as an electrolyte.

Sc-doped BaZrO$_3$ has shown promising conductivity and hydration ability,[7,26] even though there are concerns about increased proton trapping compared to other dopants (proton-trapping energies: −0.296 eV for Sc, −0.196 eV for Y, −0.201 eV for In, −0.204 eV for Gd according to ref 27). The lack of comprehensive published studies of these materials does not allow for a complete assessment of their efficacy as an electrolyte in proton-conducting applications. Therefore, in this paper, we report a series of Sc-doped BaZrO$_3$ materials focusing on hydration response as a function of doping level. We showed that defect interaction/associations might account for hydration as a function of doping level.

■ EXPERIMENTAL SECTION

Synthesis of Sc/Y-Doped BaZrO$_3$ Electrolytes, X-ray Diffraction, and Scanning Electron Microscopy Characterizations. Undoped BaZrO$_3$ and different compositions of Sc-doped and Y-doped BaZrO$_3$ were prepared by solid-state reactions resulting in the compositions listed in Table 1. Stoichiometric quantities of BaCO$_3$ (Alfa Aesar, 99.8% purity), ZrO$_2$ (Alfa Aesar, 99.7% purity), and Sc$_2$O$_3$ (Aldrich, 99.9% purity) or Y$_2$O$_3$ (Alfa Aesar, 99.9% purity) were ball milled in ethanol for 24 h, dried, and calcinated at 1100 °C for 6 h to form powders.

Table 1. List of Sc-Doped and Y-Doped BaZrO$_3$ Compositions

composition	abbreviated name
BaZrO$_3$	
BaZr$_{0.9}$Sc$_{0.1}$O$_{3-\delta}$	BZSc10
BaZr$_{0.8}$Sc$_{0.2}$O$_{3-\delta}$	BZSc20
BaZr$_{0.7}$Sc$_{0.3}$O$_{3-\delta}$	BZSc30
BaZr$_{0.6}$Sc$_{0.4}$O$_{3-\delta}$	BZSc40
BaZr$_{0.9}$Y$_{0.1}$O$_{3-\delta}$	BZY10
BaZr$_{0.8}$Y$_{0.2}$O$_{3-\delta}$	BZY20
BaZr$_{0.6}$Y$_{0.4}$O$_{3-\delta}$	BZY40

X-ray diffraction (XRD, 2008 Bruker D8) was used to examine the phase purity. The chemical stability was studied by exposing the powders at 600 °C in 50% H$_2$O (water vapor pressure ($p^*_{H_2O}$), $p^*_{H_2O}$ = 0.5 atm)—Ar for 500 h. XRD was used to observe phase changes after exposure. Scanning electron microscope (SEM, JEOL 6700F) was used to examine the sintered materials.

Electrical Conductivity Measurements. For conductivity testing, samples were pressed at 375 MPa with the addition of 1 wt % NiO (Alfa Aesar, 99% purity) as a sintering aid and drops of 10 wt % PVB as a binder. NiO was used to aid the densification of the samples. However, using sintering aids decreases materials' proton concentration and conductivity.[28,29] These effects are assumed to be similar for all of the studied materials of this work. Samples were sintered at 1600 °C for 5 h with a heating rate of 2 °C/min covering the samples with powder with the same composition, and an initial stage at 600 °C for 1 h to eliminate the organic binder. The density of the materials was calculated after sintering. Relative density was calculated using the theoretical density of 6.2 g/cm^3.[30] Pellets were polished, and ink made of Pd + Ag (1:3) (ESL) was used as the current collector on both sides, with Au wires as the leads. Samples were connected to an alumina testing fixture with a glass cover. The temperature was monitored by a thermocouple next to the samples. Air and 5% H$_2$−Ar were used as the testing gases. Wet conditions were obtained by flowing the gases through a bubbler at room temperature to obtain a content of ∼2.7% H$_2$O ($p^*_{H_2O}$ = 0.027 atm) or through a temperature-controlled humidifier for 5% H$_2$O ($p^*_{H_2O}$ = 0.05 atm). The isotope effect was studied by passing air through a bubbler at room temperature containing 100% D$_2$O to obtain a content of ∼2.7% D$_2$O ($p^*_{D_2O}$ = 0.027 atm). Conductivity was measured by electrochemical impedance spectroscopy (EIS, Solartron 700E) with 20 mA of amplitude from 0.1 Hz to 10^6 Hz.

Transference Number Calculations. Transference numbers, t_i, were calculated by the electromotive force measurement method in a concentration cell by[31−33]

$$t_i = \frac{OCV_{measured}}{EMF_{theoretical}} \quad (2)$$

where OCV$_{measured}$ corresponds to the measured open circuit voltage and EMF$_{theoretical}$ corresponds to the theoretical electromotive force, which was calculated by[31−33]

$$EMF_{theoretical} = (t_{OH_O^\bullet} + t_{V_O^{\bullet\bullet}})\frac{RT}{4F}\ln\frac{p_{O_2}^{II}}{p_{O_2}^{I}} + t_{OH_O^\bullet}\frac{RT}{2F}\ln\frac{p_{H_2O}^{I}}{p_{H_2O}^{II}} \quad (3)$$

where $t_{OH_O^\bullet}$ is the proton transport number, $t_{V_O^{\bullet\bullet}}$ is the oxygen vacancy transport number, R is the gas constant, T is the temperature, and F is the Faraday constant.

A pellet with Pd + Ag (1:3) ink (ESL) as an electrode was sealed in an alumina testing fixture using a glass powder sealant. The temperature was monitored by a thermocouple placed next to the sample. Transport numbers were calculated at 400, 500, and 600 °C. Each side of the pellet was exposed to different chemical gradients. For proton defect transference number, the samples were exposed to a fixed oxygen concentration and a water gradient (9.7% O$_2$, $p_{H_2O}^{II}/p_{H_2O}^{I}$: 5% H$_2$O ($p^*_{H_2O}$ = 0.05 atm)/2.7% H$_2$O ($p^*_{H_2O}$ = 0.027 atm)). For ionic transference numbers, the samples were exposed to a fixed water concentration and an oxygen gradient (2.7% H$_2$O ($p^*_{H_2O}$ = 0.027 atm), $p_{O_2}^{II}/p_{O_2}^{I}$: 13.1% O$_2$/9.9% O$_2$). Corrected transference numbers were calculated by considering the effect of polarization resistance[33] by

$$t_i = 1 - \frac{R_{Ohmic}}{R_T}\left(1 - \frac{OCV_{measured}}{EMF_{theoretical}}\right) \quad (4)$$

where R_{Ohmic} corresponds to the Ohmic resistance and R_T corresponds to the total resistance.
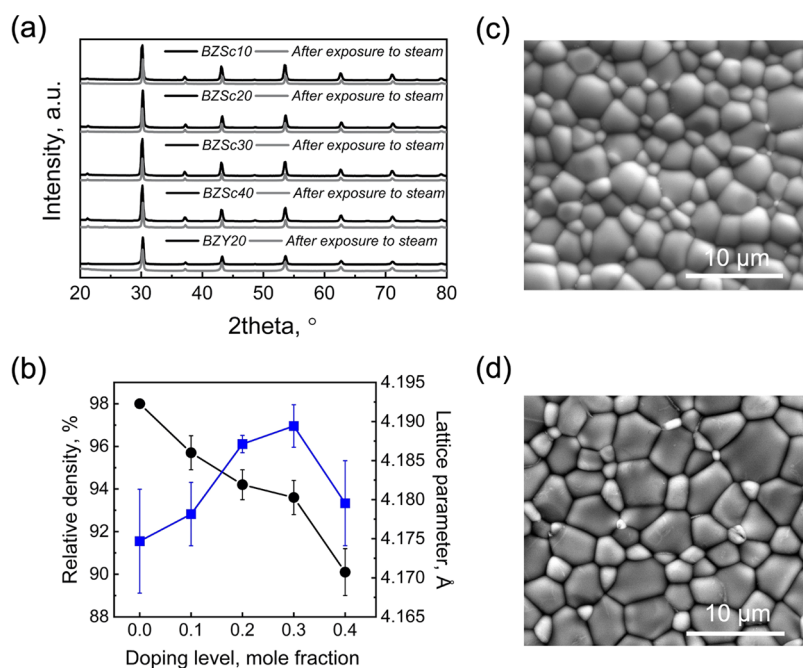
Figure 2. Characterization of Sc-doped and Y-doped BaZrO₃. (a) X-ray diffraction patterns of the as-prepared and after 500 h of exposure to 50% H₂O ($p^*_{H_2O}$ = 0.5 atm)−Ar at 600 °C for BZSc10, BZSc20, BZSc30, BZSc40, and BZY20. (b) Lattice parameter *a* and relative density of sintered materials as a function of the doping level. (c) Scanning electron microscopy image of BZSc20. (d) Scanning electron microscopy image of BZY20.

Water content was obtained by flowing the gas through a room-temperature bubbler to 2.7% H₂O ($p^*_{H_2O}$ = 0.027 atm) or a temperature-controlled humidifier for 5% H₂O ($p^*_{H_2O}$ = 0.05 atm). EIS was used to obtain R_{Ohmic}, and linear sweep voltammetry from 0 to 0.001 V was used to obtain R_T from the slope of the current−voltage curve.

Proton Concentration Calculations. Thermogravimetric analysis (TGA) measured the water uptake as a function of temperature (Netzsch STA 449 F3 Jupiter, with water vapor generator ASTEAM DV2). Powder samples were dried at 1100 °C for 1 h and cooled to 900 °C in nitrogen. Then, 10% H₂O−N₂ ($p^*_{H_2O}$ = 0.1 atm) or 5% H₂O−N₂ ($p^*_{H_2O}$ = 0.05 atm) was introduced while keeping a constant temperature to allow for weight change equilibration. After equilibration, the temperature was reduced to 300 °C, with equilibration periods every 50 °C. All measurements were corrected for buoyancy. According to the hydration reaction, eq 1, 2 moles of proton defects are formed for every mole of water incorporated into the lattice. Then, by assuming that all weight change is due to the water uptake, the proton concentration, $c_{OH^\bullet_O}$ (mole fraction), can be calculated according to[34]

$$c_{OH^\bullet_O} = \frac{\text{mass } H_2O \text{ uptake}}{\text{molar mass } H_2O} \times \frac{2 \text{ mol } OH^\bullet_O}{1 \text{ mol } H_2O} \times \frac{\text{molar mass sample}}{\text{mass sample}}$$

(5)

where the mass water uptake corresponds to the equilibrium mass change achieved at each temperature to the mass of the dry sample at 1100 °C.

The hydration equilibrium constant, K_w, at each temperature, was calculated by

$$K_w = \frac{4c_{OH^\bullet_O}^2}{P_w(c_x - c_{OH^\bullet_O})(6 - c_x - c_{OH^\bullet_O})}$$

(6)

where c_x corresponds to the doping level and P_w to the water concentration. The hydration enthalpy, ΔH_{hyd}, and entropy, ΔS_{hyd}, were calculated by

$$\ln K_w = -\frac{\Delta H_{hyd}}{RT} + \frac{\Delta S_{hyd}}{R}$$

(7)

Diffuse Reflectance Fourier Transform Spectroscopy. Diffuse reflectance Fourier transform spectroscopy (DRIFTS, Nicolet iS50, Thermo Fisher with a Praying Mantis Diffuse Reflection Accessory) was used to measure the evolution of the OH⁻ stretching band during dehydration. First, samples were dried at 550 °C for 1 h with dry He. Then, the temperature was decreased to 150 °C, and water was introduced by passing He through a bubbler at room temperature for 2 h. After hydration, the cell was flushed for 1 h with dry He at 150 °C. DRIFTS spectra were collected while heating every 50 °C until 550 °C keeping each temperature steady for 20 minutes.

Temperature-Programmed Desorption. Temperature-programmed desorption (TPD) was used to study the dehydration behavior of the materials. 100 mg of each sample was placed between wool in a tubular quartz reactor held by a glass frit. The temperature was monitored by a thermocouple placed inside the reactor. First, the temperature was increased to 800 °C to dehydrate the sample under Ar. Next, samples were hydrated during cooling to 50 °C with Ar passed through a bubbler at room temperature. The temperature was kept at 50 °C for 1 h, continuing with the hydration. Then, samples were flushed with dry Ar for 1 h at 50 °C. The H₂O−TPD was performed from 50 to 800 °C with a heating rate of 4 °C/min. The exhaust gas was monitored using online mass spectroscopy (OmniStar gas analysis system, GSD 320 O1, with a quadrupole mass spectrometer MS, QMG 220).

Positron Annihilation Lifetime Spectroscopy. Positron annihilation lifetime spectroscopy (PALS) was conducted using a TechnoAP digital spectrometer (real-time digital signal processor board, APV8702-8, with two channels, 3 GHz data sampling, and 8-bit resolution). Two fast scintillation detectors were used (BAF₂ cylindrical crystals built-in H3378-51 photomultiplier tubes, Hamamatsu Photonics). The shorter time-scale acquisition mode was used up to 70 ns range with 0.01042 ns/channel and about 1 million or more counts for each spectrum. Measurements were conducted using a sandwich arrangement where a sealed in Ti thin film with a 12.5-micron thick positron source (²²Na, 50 mCi, Eckert & Ziegler Isotope Products) was sandwiched in between two sintered pellets (Ø > 10 mm, thickness > 1 mm) of sample material.[35] Data analysis was
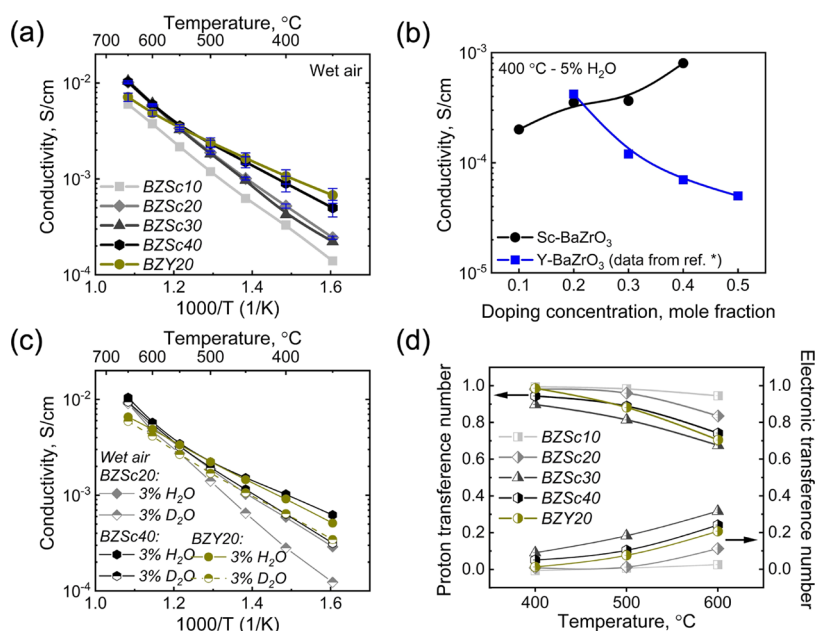
Figure 3. Conductivity and electronic conduction of a series of Sc-doped BaZrO$_3$. (a) Total conductivity in 3% H$_2$O ($p^*_{H_2O}$ = 0.03 atm)−air. (b) Comparison of total conductivity at 400 °C and 5% H$_2$O ($p^*_{H_2O}$ = 0.05 atm)−H$_2$ of Sc- and Y-doped BaZrO$_3$ versus doping concentration. * Y-doped BaZrO$_3$ data reproduced from ref 6. (c) Isotope effect: conductivity of BZSc20, BZSc40, and BZY20 in 3% H$_2$O−air and in 3% D$_2$O−air. (d) Protonic and electronic transference numbers as a function of temperature for the Sc-doped BaZrO$_3$ materials and BZY20.

conducted using the Kansy LT 9.2 analysis program with deconvolution (χ^2 goodness-of-fit $\approx$ 1, S/N $\approx$ 0.1) into three discrete lifetimes without source correction with the intensities normalized to 100% according to

$$n(t) = I_1 \exp(-t/\tau_1) + I_2 \exp(-t/\tau_2) + I_3 \exp(-t/\tau_3) \quad (8)$$

where $n(t)$ corresponds to the counts; t corresponds to the time; and I_1, I_2, and I_3 correspond to the intensity of bulk annihilation, positron trapping, and positronium formation, respectively. τ_1, τ_2, and τ_3 correspond to the lifetime of bulk annihilation, positron trapping, and positronium formation.

Sintered pellets were prepared as described in the Electrical Conductivity Measurements section. Hydrated samples were additionally treated at 300 °C for 24 h in 10% H$_2$O ($p^*_{H_2O}$ = 0.1 atm)−Ar before the measurements.

Density Functional Theory Computations. Proton migration in X-doped BaZrO$_3$ (X = Sc, Y) was studied by plane-wave density functional theory (DFT) using the Vienna Ab initio Simulation Package (VASP 6.1.2).[36−38] The generalized gradient approximation (GGA) of the Perdew−Burke−Ernzerhof (PBE) function was selected to parametrize exchange−correlation potentials. X-doped BaZrO$_3$ bulk models were created based on cubic BaZrO$_3$ unit cells. To accommodate dopants, 2 × 2 × 2 supercells containing 40 atoms were constructed. The concentration of X in X-doped BaZrO$_3$ was 25 mol %, which mimicked the composition of BZSc20 and BZY20 synthesized in experiments. We considered possible doping sites and ran geometry optimization calculations for those structures. The most stable one was chosen for the study. Proton migration in X-doped BaZrO$_3$ was investigated using Ba$_8$Zr$_6$X$_2$O$_{24}$H and Ba$_8$Zr$_6$X$_2$O$_{24}$H$_2$ supercells, representing different hydration levels. The proton migration barrier was investigated by the climbing-image nudged elastic band (CI-NEB) method with an image of 6. All calculations were performed in a spin-polarized fashion with a kinetic cutoff energy of 500 eV. A Γ-centered 4 × 4 × 4 k-point mesh was used for Brillouin zone integration. The calculation criteria for electronic self-consistency and Hellmann−Feynman forces were set as <1 × 10^{-5} eV and <0.02 eV/Å, respectively.

RESULTS AND DISCUSSION

Material Characterization. The phase purity of powder samples was examined, showing pure phase (Figure 2a). The lattice parameter, a, changed with respect to the doping level (Figure 2b). The lattice expanded by incorporating Sc up to 30 mol % of doping, while it decreased for BZSc40. The change in the lattice parameter further supports the incorporation of Sc into the lattice. In contrast, the decrease of the lattice parameter for BZSc40 can be explained by the formation of more oxygen vacancies.[39,40] All samples resulted stable in 50% H$_2$O ($p^*_{H_2O}$ = 0.5 atm)−Ar at 600 °C for 500 h with no visible new phase formation (Figure 2a). Finally, sintered materials had their relative density decreased with increasing doping concentration in Sc-doped BaZrO$_3$ (Figure 2b). The relative density of BZY20 was 95.5 ± 0.5%. Figure 2c,d shows the SEM for representative BZSc20 and BZY20, respectively. Sintered materials had an average grain size of 4−6 μm and smaller grains with an average size of 1.5−2 μm.

Dopant Effect on Proton Conductivity and Proton Concentration. The total conductivities of Sc-doped BaZrO$_3$ were measured in wet air conditions to study the dependence of the conductivity as a function of the Sc doping level (10−40 mol %). As seen in Figure 3a, the Sc dopant has an evident positive effect on the conductivity of BaZrO$_3$. BZSc40 had the highest conductivity in the studied Sc doping range between 350 and 650 °C. At the higher-temperature region (550−650 °C), the conductivities of BZSc20, BZSc30, and BZSc40 were either similar to or higher than the conductivity of BZY20. At temperatures lower than 550 °C, BZSc40 had significantly higher conductivity than other Sc-doped BaZrO$_3$ materials. However, at temperatures lower than 450 °C, BZY20 had higher conductivity in wet air. The activation energies between 450 and 650 °C were 0.66 eV for BZSc10, 0.69 eV for BZSc20, 0.72 eV for BZSc30, 0.61 eV for BZSc40, and 0.44 eV for BZY20. These results suggest that Sc-doped BaZrO$_3$ materials
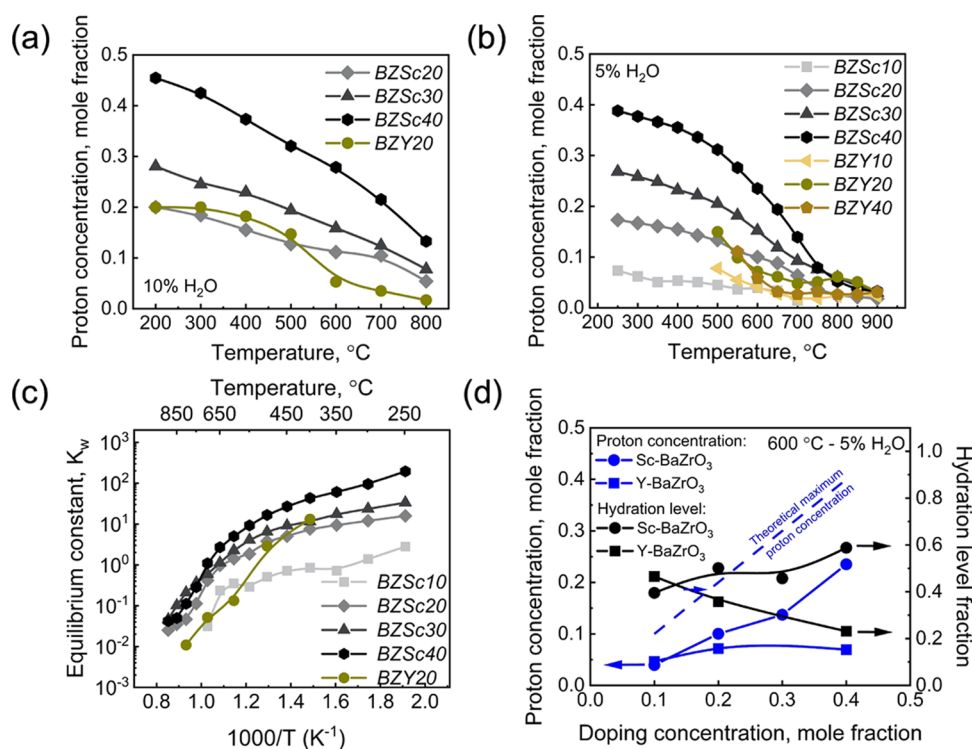
Figure 4. Hydration of Sc-doped and Y-doped $BaZrO_3$. (a) Proton concentration as a function of temperature in 10% H_2O ($p^*_{H_2O}$ = 0.1 atm)−N_2. (b) Proton concentration as a function of temperature in 5% H_2O ($p^*_{H_2O}$ = 0.05 atm)−N_2. (c) Hydration equilibrium constants. (d) Comparison of proton concentration and hydration level (actual proton concentration/theoretical maximum proton concentration) at 600 °C and 5% H_2O ($p^*_{H_2O}$ = 0.05 atm)−N_2 of Sc- and Y-doped $BaZrO_3$ versus doping concentration.

can be used in high-temperature (>500 °C) applications and that BZSc40 could be better used in low-temperature applications (<500 °C). The conductivity of Sc-doped $BaZrO_3$ increased with increasing doping levels (Figure 3b), while the trend is the opposite for Y-doped $BaZrO_3$.[6] The doping level of Sc-doped $BaZrO_3$ with the highest conductivity is inconclusive as compositions with doping higher than 40 mol % were not studied. Nevertheless, previous work showed that the conductivity of heavily Sc-doped $BaZrO_3$ (60 mol %) was higher than that of BZSc20,[26] suggesting that for highly dense and mechanically stable samples, the conductivity shows a positive trend with respect to increasing Sc doping levels.

Electron holes can be formed in an oxygen-containing atmosphere,[41,42] and electron−hole conduction can contribute to the total conductivity under oxidizing conditions. Hence, it is necessary to show that proton defects are the dominant charge carriers of doped $BaZrO_3$. If so, the conductivity in H_2O−air should be higher than that of D_2O−air due to the heavier $OD_o^\bullet$ defects. The kinetic isotope effect was studied, resulting in lower conductivities in D_2O−air than in H_2O−air (Figure 3c). The isotope effect increased with decreasing temperature with values of σ_{H_2O} − air/σ_{D_2O-air} ≈ 1.02−2.3 for temperatures between 350 and 650 °C. Such values suggest that proton migration was by the proton-hopping mechanism.[43,44] In addition, the electronic transference numbers in oxidizing conditions were also studied (Figure 3d). The protonic transference numbers decreased with increasing temperature for all materials. At the same time, their trend with doping levels in Sc-doped $BaZrO_3$ suggests that doping decreases the proton transference numbers. The calculated electronic transference numbers show an increasing trend with

increasing temperature. Finally, all studied materials had protonic transport numbers close to unity at 400 °C.

The proton concentration was studied in 10% H_2O ($p^*_{H_2O}$ = 0.1 atm) (Figure 4a) and 5% H_2O ($p^*_{H_2O}$ = 0.05 atm) (Figure 4b). The proton concentration decreased with the temperature for all materials and with lower steam concentration reaching high proton concentration at the lowest temperature studied (T < 400 °C). At higher temperatures (T > 400 °C), the proton concentration decreased significantly, having samples with higher doping levels the higher proton concentrations. Hydration energies were calculated from their equilibrium constants, K_w, using a high-temperature range of T > 600 °C (Figure 4c, Table S1). Nonlinear isotherms can be observed for the complete temperature range. Such nonlinear behavior has been previously described.[7,45] BZSc20 and BZSc40 had the most favorable hydration enthalpy (−131 kJ/mol), while the hydration enthalpy of 20, 30, and 40 mol % Sc-doped $BaZrO_3$ materials was more exothermic than the hydration enthalpy of BZY20 (−96 kJ/mol).

We can infer that increasing doping levels does not hinder the hydration of Sc-doped $BaZrO_3$ materials. The hydration level defined as the actual proton concentration over the theoretical maximum proton concentration of the Sc-doped $BaZrO_3$ and Y-doped $BaZrO_3$ at 600 °C and 5% H_2O ($p^*_{H_2O}$ = 0.05 atm) shows that hydration was more favorable for BZSc40 than the rest of the studied Sc-doped $BaZrO_3$ materials (Figure 4d). On the other hand, as the doping level increased for Y-doped $BaZrO_3$, the hydration level was reduced. While other factors could explain the difference in the conductivity and hydration trend with doping levels, such as the local
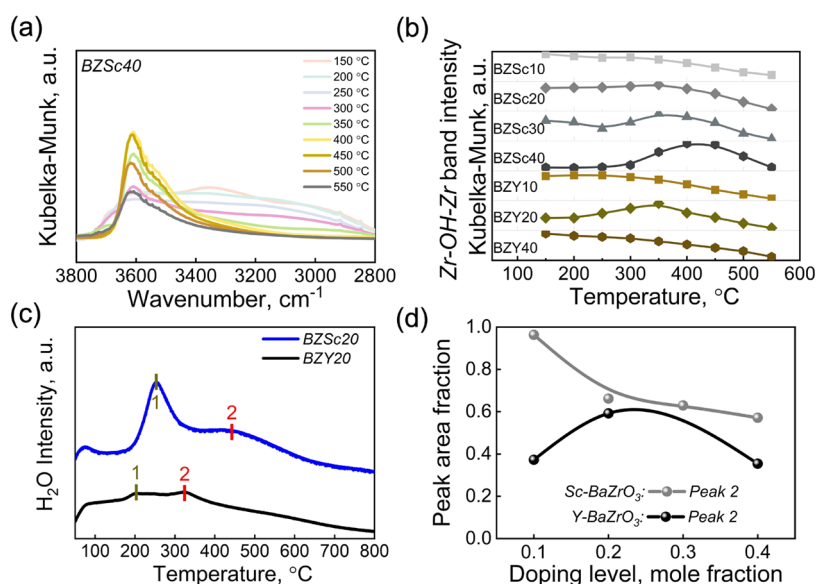
Figure 5. Effect of doping on the dehydration of doped $BaZrO_3$. (a) DRIFTS spectra of BZSc40 during dehydration showing the local environment for protons. The band around 3610 cm^{-1} can be assigned to OH$^-$ from Zr−OH−Zr while the band around 3350 cm^{-1} to OH$^-$ from X−OH−Zr where X is the dopant atom.[51] (b) Zr−OH−Zr band intensity as a function of dehydration temperature (Kubelka−Munk intensities are vertically translated). (c) H_2O−TPD spectra as a function of temperature for BZSc20 and BZY20. The peaks below 100 °C correspond to the vaporization of physically adsorbed water, while Peaks 1 and 2 correspond to water from the endothermic material dehydration: $2OH_o^{\bullet} \leftrightarrow H_2O + V_o^{\bullet\bullet} + O_O^{\times}$. (d) Peak 2 area fraction as a function of doping concentration for Sc-doped $BaZrO_3$ and Y-doped $BaZrO_3$.

structure[10−12,46−48] and dopant characteristics,[6,9,27,49,50] we will focus on the effect of proton−dopant associations on the hydration ability of the materials. We then explored why the hydration on Sc-doped $BaZrO_3$ tends to be enhanced compared to Y-doped $BaZrO_3$ and the possible effects of higher hydration on proton conduction. We started with exploring the possible influences of proton−dopant associations, i.e., proton trapping, on the hydration ability of Sc-doped $BaZrO_3$ and Y-doped $BaZrO_3$ by studying the material dehydration.

Proton Defect Characterization via Dehydration. DRIFTS was used to study the evolution of the OH$^-$ stretching band (3800−3000 cm^{-1}) during dehydration in dry He after hydration in 3% H_2O ($p^*_{H_2O}$ = 0.03 atm)−He assuming that the local environments of the protons in the sample would result in changes on the OH$^-$ stretching band observed by DRIFTS. The spectra for BZSc40 (Figure 5a, other samples shown in Figure S1) show the shift of the OH$^-$ stretching band peak with a temperature increase from 150 to 550 °C. This band peak shift indicates two different local environments of the protons in the sample. The band peak centered around 3540−3630 cm^{-1} can be assigned to an OH$^-$ between two Zr atoms, Zr−OH−Zr,[51] while the band maximum centered around 3350 cm^{-1} can be assigned to an OH$^-$ between a Zr atom and a dopant atom (X), Zr−OH−X.[51,52] Therefore, the 3350 cm^{-1} peak intensity evolution is of significant interest since it can indicate the concentration of protons experiencing proton trapping in the electrolytes.

The peak at 3350 cm^{-1} was apparent in the temperature region from 150 to 300 °C but disappeared at higher temperatures. It was only visible in Sc-doped $BaZrO_3$ materials with high doping concentrations and only in Y-doped $BaZrO_3$ materials (Figure S1). Proton trapping is believed to be accentuated at low temperatures;[21] therefore, the presence of the 3350 cm^{-1} peak (Zr−OH−X) at low temperatures and its

subsequent disappearance at higher temperatures can be explained by the low-temperature proton-trapping effect.

The intensity of the Zr−OH−Zr peak (3540−3630 cm^{-1}) was used to characterize the dehydration (Figure 5b). The intensity of the Zr−OH−Zr peak (3540−3630 cm^{-1}) decreased as the temperature was increased for BZSc10, BZSc20, and the Y-doped $BaZrO_3$ materials. However, Sc-doped $BaZrO_3$ materials with higher doping concentrations (30 mol %, 40 mol %) showed an initial increase in intensity, with maximum intensity at about 400 °C, followed by a decrease in intensity. This could indicate that protons in proton-trapping positions (Zr−OH−X) might migrate to nontrapping positions (Zr−OH−Zr), as reported previously.[21,53] Though the increase in the intensity of the Zr−OH−Zr peak (3540−3630 cm^{-1}) with increasing temperature was not apparent in the other compounds, the possibility of the migration of protons from the trapping position to nontrapping positions with increasing temperature is plausible.

We next studied the samples by H_2O−TPD, focusing on the high-temperature water desorption that can infer the local environment for protons in the sample. The H_2O−TPD spectra for BZSc20 and BZY20 (Figure 5c) show multipeak H_2O dissociation. As observed in the literature and Figure 4a,b, the maximum hydration of the material occurs at low temperatures, while the material dehydration is evident at temperatures above ~300 °C.[7,13] Therefore, the peak below 150 °C can be assigned to the vaporization of physically adsorbed water,[54,55] leaving the high-temperature peaks to the H_2O dissociation from the lattice due to the endothermic material dehydration. Multiple peaks at higher temperatures (T > 150 °C) in the H_2O−TPD spectra suggest different proton dissociation energies. The lower-temperature peak, Peak 1 in Figure 5c, can be related to protons in chemical environments where dissociation requires less energy. The higher-temperature peak, Peak 2 in Figure 5c, involves more protons in
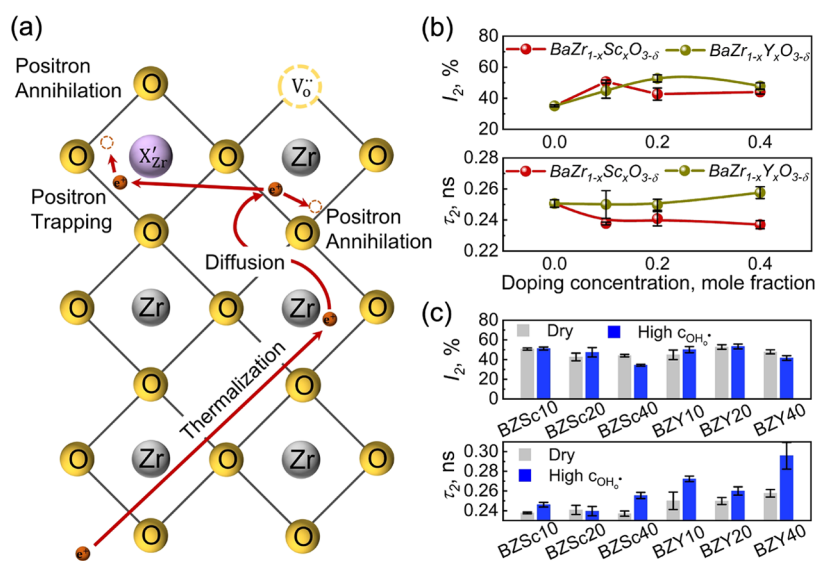
Figure 6. Positron annihilation lifetime spectroscopy for the study of proton trapping in doped BaZrO$_3$. (a) Schematic of positron annihilation in doped BaZrO$_3$: positron penetrates sample, thermalizes, and diffuses until annihilation with electrons. Positrons can take longer to annihilate due to, for example, the trapping in negatively charged defects. (b) Positron-trapping intensity, I_2, and lifetime, τ_2, as a function of doping for Sc-doped BaZrO$_3$ and Y-doped BaZrO$_3$. (c) Comparison of positron-trapping intensity, I_2, and lifetime, τ_2, for dry and hydrated Sc-doped BaZrO$_3$ and Y-doped BaZrO$_3$.

chemical environments where dissociation requires higher energy.

The remaining materials showed similar H$_2$O−TPD spectra with two high-temperature peaks (Figure S2). The analysis of Peak 2 area fraction (Peak 2 area over the total area of Peak 1 and Peak 2) (Figure 5d) showed that for Sc-doped BaZrO$_3$ materials, protons from Peak 2 decreased in concentration with increasing doping level. For Y-doped BaZrO$_3$ materials, the peak area fraction for Peak 2 showed a maximum of 20 mol % of doping and decreased with increasing doping concentration. The results suggest that Sc-doped BaZrO$_3$ has the potential to retain more protons at a higher temperature (higher Peak 2 area fractions) than Y-doped BaZrO$_3$.

Protons in positions of proton trapping, Zr−OH−X, might be the main component of Peak 1 as the dehydration of the material will form a more stable oxygen vacancy near a dopant atom, Zr−V$_o^{\bullet\bullet}$−X, than in between zirconium atoms, Zr−V$_o^{\bullet\bullet}$−Zr.[56] Therefore, protons not in proton-trapping positions might be the main component of Peak 2. In addition, according to DRIFTS results, protons that required higher energy to dissociate (Peak 2) might include protons initially in a proton-trapping position, Zr−OH−X, that migrated to Zr−OH−Zr as the temperature was increased. Thus, proton trapping could influence the level of hydration at high temperatures.

Proton-Trapping Study by Positron Annihilation Lifetime Spectroscopy. As discussed in the previous section, material dehydration was influenced by proton trapping and proton migration. We next expand the study of the proton trapping on hydrated Sc-doped BaZrO$_3$ and Y-doped BaZrO$_3$. A better understanding of the nature of proton trapping as a function of doping level requires using special techniques such as nuclear magnetic resonance,[21,22] quasielastic neutron scattering,[48,57] or modeling and computational work.[18,58] PALS has been used to study the electron structure of ceramics and oxides on the nanoscale.[35,59−64] According to PALS theory, the positively charged positrons penetrate inside the bulk of the samples, thermalize, and diffuse until they

annihilate with electrons[35,61] (Figure 6a). The presence of lattice dislocations or negatively charged defects affects positrons since they tend to be trapped in low electron density volumes.[61] Therefore, structural defects, open pores, and negative or neutral vacancies increase the positrons' lifetime before annihilation.[61] Oxygen vacancies do not trap positrons due to their positive charge.[65] For highly dense doped BaZrO$_3$ materials, the presence of the negatively charged areas induced by dopants could act as positron-trapping sites (Figure 6a) and hence contribute to the positron-trapping intensity (I_2) and the positron-trapping lifetime (τ_2). The possible Ba vacancies formed[66] and the space charge region outside grain boundaries can contribute to positron trapping.[59,67]

The PALS spectra for BZSc20 (Figure S3) show the response broken down into bulk annihilation, positron trapping, and positronium formation contributions. Significant contributions, more than 1%, were observed only for bulk annihilation (I_1 and τ_1) and positron trapping (I_2 and τ_2). When compared to undoped BaZrO$_3$, doping modified the positron-trapping intensity of BaZrO$_3$ (Figure 6b). The source of positron trapping on undoped BaZrO$_3$ could correspond to positron trapping at the space charge region along grain boundaries and on Ba vacancies.[59,67] The evolution of I_2 as a function of doping level (Figure 6b) demonstrates that dopant atoms increased the positron-trapping sites as I_2 increased, although not linearly, with the doping level for Sc-doped BaZrO$_3$ and Y-doped BaZrO$_3$. The effects of positron trapping as a function of doping concentration were nonlinear since doping may modify the positron-trapping site's character.[65]

On the other hand, τ_2 decreased for Sc-doped BaZrO$_3$ as a function of doping due to the higher electron density at the positron-trapping site. At the same time, τ_2 increased for Y-doped BaZrO$_3$ as a function of doping, suggesting a lower electron density at the positron-trapping site.[62] The longer τ_2 for Y-doped BaZrO$_3$ materials compared to Sc-doped BaZrO$_3$ is caused by different valence/core electron densities related to
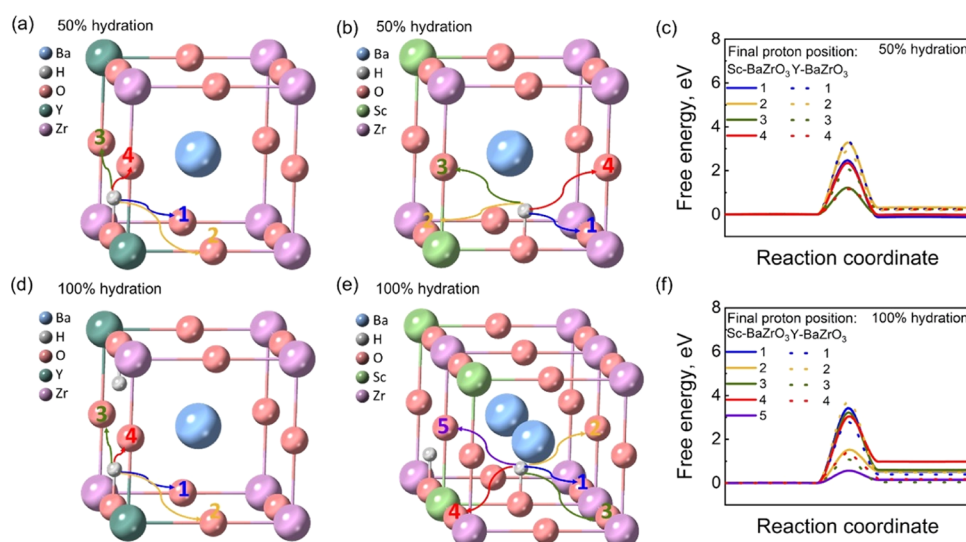
Figure 7. Density functional theory calculation for proton migration of 25 mol % Y- or Sc-doped $BaZrO_3$. Proton migration paths in the lattice at 50% of hydration for (a) Y-doped $BaZrO_3$ and (b) Sc-doped $BaZrO_3$. (c) Potential energy profiles for the proton migration paths in panels (a) and (b) for Sc-doped $BaZrO_3$ and Y-doped $BaZrO_3$. Proton migration paths in the lattice at 100% of hydration for (d) Y-doped $BaZrO_3$ and (e) Sc-doped $BaZrO_3$. (f) Potential energy profiles for the proton migration paths in panels (d) and (e) for Sc-doped $BaZrO_3$ and Y-doped $BaZrO_3$.

the bigger positive core of Y with the same amount of valence electrons as Sc.

We then studied fully hydrated materials and compared I_2 and τ_2, which represent positron-trapping intensity and lifetime, respectively, to that of dry samples (Figure 6c). τ_2 increased for almost all samples after hydration. On the other hand, I_2 slightly increased or remained the same in the error range for low doping concentrations (at 10 and 20 mol %). However, it decreased significantly for high doping concentrations (40 mol %) in hydrated specimens.

We propose that protons might deflect positrons due to their positive charge, thus causing the positron-trapping diffusion pathway to lengthen. The more extended diffusion pathway will increase the positron-trapping lifetime (τ_2), i.e., it takes longer for the positron to reach the positron-trapping site. Similar behavior was reported in the literature where the hydrogen uptake by metals increased the positron lifetime and decreased the electron density of the material since some of the electrons may be immobilized by the influx of protons.[68]

At the same time, if the positron pathway is lengthened, the probability of positrons being trapped could decrease since positrons might annihilate with delocalized electrons before reaching the trapping sites. In this case, the positron-trapping intensity (I_2) might decrease from I_2 from dry samples. This was the case for BZSc40 and BZY40, where τ_2 increased significantly.

On the other hand, there is a contrary effect since protons might also neutralize some of the material electrons, making them unavailable for positron annihilation. This allows more positrons to reach the trapping sites so that I_2 might increase compared to I_2 from dry samples. This was the case for BZSc10, BZSc20, BZY10, and BZY20. Therefore, the change in the trapping lifetime (τ_2) in hydrated specimens would be due to several effects: the surge in the presence of positively charged protons, the altering of the positron pathway to the trapping sites, and the altering of the trapping sites, i.e., dopant defects, by the protons. Future studies are required to develop the present theory and characterize proton trapping by PALS.

Proton-Trapping Effect on $BaZrO_3$ Hydration. The previous results indicate that proton trapping might occur during the hydration and dehydration of Sc-doped $BaZrO_3$ and Y-doped $BaZrO_3$. The results also suggest that these processes appear more strongly on Sc-doped $BaZrO_3$. The effect of proton trapping on hydration was examined previously. Literature has predicted that the ratio of the trapping energy of oxygen vacancies over the trapping energy of protons by the dopant could predict the material hydration enhancement or inhibition.[14] In previous work, Sc doping enhanced the hydration of $BaZrO_3$ compared to Y, which impeded the hydration.[14] While it has been shown that Sc doping leads to stronger proton trapping,[27,69,70] the oxygen vacancy trapping energy for Sc is lower than for bigger dopant atoms,[69] resulting in favorable ratios of trapping energy of oxygen vacancies over that of protons, which, in turn, predicts favorable hydration even at increasing doping levels.[14]

Precisely how the proton trapping and migration interfere in the material hydration is not clear. Nonetheless, the proton trapping in Sc-doped $BaZrO_3$ positively correlated with material hydration. However, the increase in conductivity with the doping level in Sc-doped $BaZrO_3$ requires more insight. Sc-doped $BaZrO_3$ and Y-doped $BaZrO_3$ proton concentrations increased with doping concentrations, while the increase was even higher for Sc-doped $BaZrO_3$. Still, such a proton concentration increase might not be enough to account for the conductivity increase with the doping level observed in Sc-doped $BaZrO_3$.

Effect of Hydration on the Proton Conduction. A proton experiencing trapping shows reduced conduction compared to a nontrapped proton.[21] While previous work has suggested that percolation channels could appear in samples with a high doping concentration and hence facilitate the proton conduction,[58] we are interested in studying the effect of enhanced hydration, i.e., higher proton concentration, on the conduction of a proton experiencing proton trapping by density functional theory. To that end, a $2 \times 2 \times 2$ supercell was constructed, representing 25 mol % of doping ($Ba_8Zr_6X_2O_{24}$, where X represents Sc or Y). Three supercells

(supercells A, B, and C) were created for each composition to investigate the distribution of dopant atoms. Details about the lattice structure of these supercells and relative energy differences can be found in Figures S4 and S5 and Table S2. The lattice structure of supercell C, which exhibits the lowest energy for both compositions, was used in subsequent simulations. Including Y or Sc cations at Zr^{4+} sites disrupt the electronic balance, which will be compensated by the formation of oxygen vacancies. Owing to lattice symmetry, three nonequivalent oxygen vacancy sites exist, as depicted in Figure S6a. The formation energy of oxgyen vacancies for $Ba_8Zr_6X_2O_{23}$ (X = Sc or Y) with different oxygen vacancy sites was calculated. It was found that oxygen vacancies tend to form on site 1 in Sc-doped $BaZrO_3$, whereas oxygen vacancies show a preference for site 3 in Y-doped $BaZrO_3$ (Figure S6b). The reaction energy and migration barrier for the conduction of a proton in a trapping position were calculated as a function of hydration level, considering that for the supercell, the complete hydration of the material corresponds to two protons (100% hydration). In contrast, incomplete hydration corresponds to one proton (50% hydration).

In our analysis of incomplete hydration, we considered the migration of a proton from its trapping site to four adjacent oxygen sites. Figure 7a employs a quarter of the Y-doped $BaZrO_3$ supercell for demonstration. Oxygen sites in the (001) plane were designated sites 1 and 2, while those in the (100) plane were labeled sites 3 and 4. The four potential proton migration pathways in Sc-doped $BaZrO_3$ were illustrated in Figure 7b using the same method. The activation energy for the migration of a proton in a trapping position is slightly lower in Y-doped $BaZrO_3$ (1.16 eV) than in Sc-doped $BaZrO_3$ (1.22 eV), as shown in Figure 7c. However, if the hydration level is increased, the local environment of trapped protons would be changed by neighboring protons. To explore neighboring protons' absorption sites, we investigated the hydration process in Sc-doped $BaZrO_3$ and Y-doped $BaZrO_3$ (Figure S7). The most stable configuration, possessing the lowest hydration energy, was chosen for the exploration of proton migration in fully hydrated scenarios. For Y-doped $BaZrO_3$, the neighboring proton prefers a second nearest neighbor site, resulting in four potential migration pathways (Figure 7d).

Conversely, the neighboring proton demonstrated a preference for the first nearest neighbor site in Sc-doped $BaZrO_3$. This preference reduces the lattice symmetry, thus providing five nonequivalent proton migration pathways (Figure 7e). We observed that the activation energy for a proton's migration in a trapping position remarkably drops for Sc-doped $BaZrO_3$ (0.57 eV), see Figure 7f, compared with activation energy for proton conduction for incomplete hydration. The influence of a neighboring proton is less pronounced in Y-doped $BaZrO_3$ due to the increased distance between two protons. This distant neighboring proton only marginally reduces the migration barrier to 1.08 eV. The results are consistent with a previous computational report that suggested a positive effect of proton–proton interactions through a trap-filling mechanism that increases the proton diffusivity on Y-doped $BaZrO_3$.[71] The positive proton–proton interaction decreased the activation energy more significantly for Sc-doped $BaZrO_3$ than for Y-doped $BaZrO_3$. This partially explains why the conductivity of Sc-doped $BaZrO_3$ increases with doping as opposed to Y-doped $BaZrO_3$. The hydration is improved for high doping levels in Sc-doped $BaZrO_3$, and the

activation energy for proton migration is reduced. However, for Y-doped $BaZrO_3$, high doping levels do not substantially enhance the hydration of the material, and the activation energy for proton migration in a highly hydrated material is not reduced significantly. Both factors could end up limiting the conductivity of highly doped Y-doped $BaZrO_3$ and enhancing the conductivity of highly doped Sc-doped $BaZrO_3$.

■ CONCLUSIONS

This work investigated the origin of increased proton conductivity in Sc-doped $BaZrO_3$ materials with different doping levels. We revealed that the conductivity increased with high Sc doping levels and that the hydration ability of the material did not seem to be hindered by higher doping concentrations, as opposed to Y-doped $BaZrO_3$. It was proposed that the proton trapping influences the material hydration and dehydration, resulting in higher hydration of Sc-doped $BaZrO_3$ materials. However, the mechanism is not completely clear. Moreover, DFT calculations showed that the proton migration is boosted for highly hydrated Sc-doped $BaZrO_3$ compared to Y-doped $BaZrO_3$. This positive feature could expand the future work on Sc-doped $BaZrO_3$ and focus on the application of these materials in intermediate-temperature applications. Furthermore, positron annihilation lifetime spectroscopy was used to explore proton trapping for the first time. The results showed the promise of this technique to characterize dense proton conductors.

■ ASSOCIATED CONTENT

ⓈI Supporting Information

The Supporting Information is available free of charge at https://pubs.acs.org/doi/10.1021/acs.chemmater.3c00531.

DRIFTS results, H_2O–TPD results, PALS spectra for BZSc20, and DFT details (PDF)

■ AUTHOR INFORMATION

Corresponding Authors

Hanping Ding − *Energy and Environment Science & Technology, Idaho National Laboratory, Idaho Falls, Idaho 83415, United States; School of Aerospace and Mechanical Engineering, University of Oklahoma, Norman, Oklahoma 73019, United States*; Email: hding@ou.edu

Hongmei Luo − *Department of Chemical and Materials Engineering, New Mexico State University, Las Cruces, New Mexico 88003, United States;* ⓞ orcid.org/0000-0002-9546-761X; Email: hluo@nmsu.edu

Dong Ding − *Energy and Environment Science & Technology, Idaho National Laboratory, Idaho Falls, Idaho 83415, United States;* ⓞ orcid.org/0000-0002-6921-4504; Email: dong.ding@inl.gov

Authors

Clarita Y. Regalado Vera − *Energy and Environment Science & Technology, Idaho National Laboratory, Idaho Falls, Idaho 83415, United States; Department of Chemical and Materials Engineering, New Mexico State University, Las Cruces, New Mexico 88003, United States*

Jagoda Urban-Klaehn − *Energy and Environment Science & Technology, Idaho National Laboratory, Idaho Falls, Idaho 83415, United States*

Meng Li − *Energy and Environment Science & Technology, Idaho National Laboratory, Idaho Falls, Idaho 83415, United States*

Zeyu Zhao − *Energy and Environment Science & Technology, Idaho National Laboratory, Idaho Falls, Idaho 83415, United States*

Frederick Stewart − *Energy and Environment Science & Technology, Idaho National Laboratory, Idaho Falls, Idaho 83415, United States*

Hanchen Tian − *Department of Mechanical and Aerospace Engineering, West Virginia University, Morgantown, West Virginia 26506, United States;* ⓘ orcid.org/0000-0003-0044-5678

Xingbo Liu − *Department of Mechanical and Aerospace Engineering, West Virginia University, Morgantown, West Virginia 26506, United States;* ⓘ orcid.org/0000-0001-8720-7175

Yanhao Dong − *Department of Nuclear Science and Engineering, Massachusetts Institute of Technology, Cambridge, Massachusetts 02139, United States;* ⓘ orcid.org/0000-0003-1224-1015

Ju Li − *Department of Materials Science and Engineering, Massachusetts Institute of Technology, Cambridge, Massachusetts 02139, United States;* ⓘ orcid.org/0000-0002-7841-8058

Meng Zhou − *Department of Chemical and Materials Engineering, New Mexico State University, Las Cruces, New Mexico 88003, United States;* ⓘ orcid.org/0000-0002-0150-445X

Complete contact information is available at:
https://pubs.acs.org/10.1021/acs.chemmater.3c00531

Notes
The authors declare no competing financial interest.

◼ REFERENCES

(1) Iwahara, H. Technological challenges in the application of proton conducting ceramics. *Solid State Ionics* **1995**, *77*, 289−298.

(2) Ding, D.; Zhang, Y.; Wu, W.; Chen, D.; Liu, M.; He, T. A novel low-thermal-budget approach for the co-production of ethylene and hydrogen via the electrochemical non-oxidative deprotonation of ethane. *Energy Environ. Sci.* **2018**, *11*, 1710−1716.

(3) Dai, L.; Wang, L.; Shao, G.; Li, Y. A novel amperometric hydrogen sensor based on nano-structured ZnO sensing electrode and CaZr0.9In0.1O3−δ electrolyte. *Sens. Actuators, B* **2012**, *173*, 85−92.

(4) Bian, W.; Wu, W.; Wang, B.; Tang, W.; Zhou, M.; Jin, C.; Ding, H.; Fan, W.; Dong, Y.; Li, J.; Ding, D. Revitalizing interface in protonic ceramic cells by acid etch. *Nature* **2022**, *604*, 479−485.

(5) Li, M.; Hua, B.; Wu, W.; Wang, L.-C.; Ding, Y.; Welander, M. M.; Walker, R. A.; Ding, D. Activating nano-bulk interplays for sustainable ammonia electrosynthesis. *Mater. Today* **2022**, *60*, 31−40.

(6) Fabbri, E.; Pergolesi, D.; Licoccia, S.; Traversa, E. Does the increase in Y-dopant concentration improve the proton conductivity of BaZr$_{1−x}$Y$_x$O$_{3−δ}$ fuel cell electrolytes? *Solid State Ionics* **2010**, *181*, 1043−1051.

(7) Kreuer, K. D.; Adams, S.; Munch, W.; Fuchs, A.; Klock, U.; Maier, J. Proton conducting alkaline earth zirconates and titanates for high drain electrochemical applications. *Solid State Ionics* **2001**, *145*, 295−306.

(8) Giannici, F.; Longo, A.; Balerna, A.; Kreuer, K.-D.; Martorana, A. Proton Dynamics in In:BaZrO3: Insights on the Atomic and Electronic Structure from X-ray Absorption Spectroscopy. *Chem. Mater.* **2009**, *21*, 2641−2649.

(9) Gilardi, E.; Fabbri, E.; Bi, L.; Rupp, J. L. M.; Lippert, T.; Pergolesi, D.; Traversa, E. Effect of Dopant−Host Ionic Radii Mismatch on Acceptor-Doped Barium Zirconate Microstructure and Proton Conductivity. *J. Phys. Chem. C* **2017**, *121*, 9739−9747.

(10) Mburu, C. W.; Gaita, S. M.; Knee, C. S.; Gatari, M. J.; Karlsson, M. Influence of Yttrium Concentration on Local Structure in BaZr1−xYxO3−δ Based Proton Conductors. *J. Phys. Chem. C* **2017**, *121*, 16174−16181.

(11) Ding, J.; Balachandran, J.; Sang, X.; Guo, W.; Anchell, J. S.; Veith, G. M.; Bridges, C. A.; Cheng, Y.; Rouleau, C. M.; Poplawsky, J. D.; et al. The Influence of Local Distortions on Proton Mobility in Acceptor Doped Perovskites. *Chem. Mater.* **2018**, *30*, 4919−4925.

(12) Giannici, F.; Shirpour, M.; Longo, A.; Martorana, A.; Merkle, R.; Maier, J. Long-Range and Short-Range Structure of Proton-Conducting Y:BaZrO3. *Chem. Mater.* **2011**, *23*, 2994−3002.

(13) Vera, C. Y. R.; Ding, H.; Peterson, D.; Gibbons, W. T.; Zhou, M.; Ding, D. A mini-review on proton conduction of BaZrO$_3$-based perovskite electrolytes. *J. Phys. Energy* **2021**, *3*, No. 032019.

(14) Putilov, L. P.; Tsidilkovski, V. I. Impact of bound ionic defects on the hydration of acceptor-doped proton-conducting perovskites. *Phys. Chem. Chem. Phys.* **2019**, *21*, 6391−6406.

(15) Takahashi, H.; Yashima, I.; Amezawa, K.; Eguchi, K.; Matsumoto, H.; Takamura, H.; Yamaguchi, S. First-Principles Calculations for the Energetics of the Hydration Reaction of Acceptor-Doped BaZrO3. *Chem. Mater.* **2017**, *29*, 1518−1526.

(16) Eisele, S.; Draber, F. M.; Grieshammer, S. The effect of ionic defect interactions on the hydration of yttrium-doped barium zirconate. *Phys. Chem. Chem. Phys.* **2021**, *23*, 4882−4891.

(17) Putilov, L. P.; Tsidilkovski, V. I. The role of deep acceptor centers in the oxidation of acceptor-doped wide-band-gap perovskites ABO$_3$. *J. Solid State Chem.* **2017**, *247*, 147−155.

(18) Toyoura, K.; Meng, W.; Han, D.; Uda, T. Preferential proton conduction along a three-dimensional dopant network in yttrium-doped barium zirconate: a first-principles study. *J. Mater. Chem. A* **2018**, *6*, 22721−22730.

(19) Kasamatsu, S.; Sugino, O.; Ogawa, T.; Kuwabara, A. Dopant arrangements in Y-doped BaZrO$_3$ under processing conditions and their impact on proton conduction: a large-scale first-principles thermodynamics study. *J. Mater. Chem. A* **2020**, *8*, 12674−12686.

(20) Kreuer, K. D. Proton-Conducting Oxides. *Annu. Rev. Mater. Res.* **2003**, *33*, 333−359.

(21) Yamazaki, Y.; Blanc, F.; Okuyama, Y.; Buannic, L.; Lucio-Vega, J. C.; Grey, C. P.; Haile, S. M. Proton trapping in yttrium-doped barium zirconate. *Nat. Mater.* **2013**, *12*, 647−651.

(22) Oikawa, I.; Takamura, H. Correlation among Oxygen Vacancies, Protonic Defects, and the Acceptor Dopant in Sc-Doped BaZrO$_3$ Studied by ^{45}Sc Nuclear Magnetic Resonance. *Chem. Mater.* **2015**, *27*, 6660−6667.

(23) Han, D.; Liu, X.; Bjørheim, T. S.; Uda, T. Yttrium-Doped Barium Zirconate-Cerate Solid Solution as Proton Conducting Electrolyte: Why Higher Cerium Concentration Leads to Better

Performance for Fuel Cells and Electrolysis Cells. *Adv. Energy Mater.* **2021**, *11*, No. 2003149.

(24) Ueno, K.; Hatada, N.; Han, D.; Uda, T. Thermodynamic maximum of Y doping level in barium zirconate in co-sintering with NiO. *J. Mater. Chem. A* **2019**, *7*, 7232−7241.

(25) Kjølseth, C.; Fjeld, H.; Prytz, Ø.; Dahl, P. I.; Estournès, C.; Haugsrud, R.; Norby, T. Space−charge theory applied to the grain boundary impedance of proton conducting BaZr0.9Y0.1O3−δ. *Solid State Ionics* **2010**, *181*, 268−275.

(26) Hyodo, J.; Kitabayashi, K.; Hoshino, K.; Okuyama, Y.; Yamazaki, Y. Fast and Stable Proton Conduction in Heavily Scandium-Doped Polycrystalline Barium Zirconate at Intermediate Temperatures. *Adv. Energy Mater.* **2020**, *10*, No. 2000213.

(27) Yamazaki, Y.; Kuwabara, A.; Hyodo, J.; Okuyama, Y.; Fisher, C. A. J.; Haile, S. M. Oxygen Affinity: The Missing Link Enabling Prediction of Proton Conductivities in Doped Barium Zirconates. *Chem. Mater.* **2020**, *32*, 7292−7300.

(28) Han, D.; Uemura, S.; Hiraiwa, C.; Majima, M.; Uda, T. Detrimental Effect of Sintering Additives on Conducting Ceramics: Yttrium-Doped Barium Zirconate. *ChemSusChem* **2018**, *11*, 4102− 4113.

(29) Huang, Y.; Merkle, R.; Maier, J. Effect of NiO addition on proton uptake of $BaZr_{1-x}Y_xO_{3-x/2}$ and $BaZr_{1-x}Sc_xO_{3-x/2}$ electrolytes. *Solid State Ionics* **2020**, *347*, No. 115256.

(30) Yamazaki, Y.; Hernandez-Sanchez, R.; Haile, S. M. High Total Proton Conductivity in Large-Grained Yttrium-Doped Barium Zirconate. *Chem. Mater.* **2009**, *21*, 2755−2762.

(31) Han, D.; Noda, Y.; Onishi, T.; Hatada, N.; Majima, M.; Uda, T. Transport properties of acceptor-doped barium zirconate by electromotive force measurements. *Int. J. Hydrogen Energy* **2016**, *41*, 14897− 14908.

(32) Bentzer, H. K.; Bonanos, N.; Phair, J. W. EMF measurements on mixed protonic/electronic conductors for hydrogen membrane applications. *Solid State Ionics* **2010**, *181*, 249−255.

(33) Liu, M.; Hu, H. Effect of Interfacial Resistance on Determination of Transport Properties of Mixed-Conducting Electrolytes. *J. Electrochem. Soc.* **1996**, *143*, L109−L112.

(34) Oishi, M.; Akoshima, S.; Yashiro, K.; Sato, K.; Mizusaki, J.; Kawada, T. Defect structure analysis of B-site doped perovskite-type proton conducting oxide $BaCeO_3$ Part 1: The defect concentration of $BaCe_{0.9}M_{0.1}O_{3-\delta}$ (M=Y and Yb). *Solid State Ionics* **2009**, *180*, 127− 131.

(35) Taylor, C. N.; Urban-Klaehn, J.; Le, T. T.; Zaleski, R.; Rimer, J. D.; Gering, K. L. Catalyst Deactivation Probed by Positron Annihilation Spectroscopy. *ACS Catal.* **2021**, *11*, 14967−14976.

(36) Kresse, G.; Hafner, J. Ab initio molecular dynamics for liquid metals. *Phys. Rev. B* **1993**, *47*, 558−561.

(37) Dong, W.; Kresse, G.; Furthmuller, J.; Hafner, J. Chemisorption of H on Pd(111): An ab initio approach with ultrasoft pseudopotentials. *Phys. Rev. B* **1996**, *54*, 2157−2166.

(38) Kresse, G.; Furthmuller, J. Efficiency of ab-initio total energy calculations for metals and semiconductors using a plane-wave basis set. *Comput. Mater. Sci.* **1996**, *6*, 15−50.

(39) Jedvik, E.; Lindman, A.; Benediktsson, Mp.; Wahnström, G. Size and shape of oxygen vacancies and protons in acceptor-doped barium zirconate. *Solid State Ionics* **2015**, *275*, 2−8.

(40) Hoedl, M. F.; Makagon, E.; Lubomirsky, I.; Merkle, R.; Kotomin, E. A.; Maier, J. Impact of point defects on the elastic properties of $BaZrO_3$: Comprehensive insight from experiments and ab initio calculations. *Acta Mater.* **2018**, *160*, 247−256.

(41) Dong, Y.; Huang, Y.; Ding, D.; Wu, W.; Yao, X.; Li, J. Chemical and structural origin of hole states in yttria-stabilized zirconia. *Acta Mater.* **2021**, *203*, No. 116487.

(42) Ding, H.; Wu, W.; Jiang, C.; Ding, Y.; Bian, W.; Hu, B.; Singh, P.; Orme, C. J.; Wang, L.; Zhang, Y.; Ding, D. Self-sustainable protonic ceramic electrochemical cells using a triple conducting electrode for hydrogen and power production. *Nat. Commun.* **2020**, *11*, No. 1907.

(43) Nowick, A. S.; Vaysleyb, A. V. Isotope effect and proton hopping in high-temperature protonic conductors. *Solid State Ionics* **1997**, *97*, 17−26.

(44) Nagao, M.; Kamiya, T.; Heo, P.; Tomita, A.; Hibino, T.; Sano, M. Proton Conduction in In3+-Doped SnP_2O_7 at Intermediate Temperatures. *J. Electrochem. Soc.* **2006**, *153*, A1604−A1609.

(45) Yamazaki, Y.; Babilo, P.; Haile, S. M. Defect Chemistry of Yttrium-Doped Barium Zirconate: A Thermodynamic Analysis of Water Uptake. *Chem. Mater.* **2008**, *20*, 6352−6357.

(46) Giannici, F.; Longo, A.; Kreuer, K.-D.; Balerna, A.; Martorana, A. Dopants and defects: Local structure and dynamics in barium cerates and zirconates. *Solid State Ionics* **2010**, *181*, 122−125.

(47) Zeudmi Sahraoui, D.; Mineva, T. Effect of dopant nature on structures and lattice dynamics of proton-conducting $BaZrO_3$. *Solid State Ionics* **2013**, *253*, 195−200.

(48) Noferini, D.; Koza, M. M.; Karlsson, M. Localized Proton Motions in Acceptor-Doped Barium Zirconates. *J. Phys. Chem. C* **2017**, *121*, 7088−7093.

(49) Han, D.; Shinoda, K.; Sato, S.; Majima, M.; Uda, T. Correlation between electroconductive and structural properties of proton conductive acceptor-doped barium zirconate. *J. Mater. Chem. A* **2015**, *3*, 1243−1250.

(50) Løken, A.; Bjørheim, T. S.; Haugsrud, R. The pivotal role of the dopant choice on the thermodynamics of hydration and associations in proton conducting $BaCe_{0.9}X_{0.1}O_{3-\delta}$ (X = Sc, Ga, Y, In, Gd and Er). *J. Mater. Chem. A* **2015**, *3*, 23289−23298.

(51) Karlsson, M.; Björketun, M. E.; Sundell, P. G.; Matic, A.; Wahnström, G.; Engberg, D.; Börjesson, L.; Ahmed, I.; Eriksson, S.; Berastegui, P. Vibrational properties of protons in hydrated $BaIn_xZr_{1-x}O_{3-x/2}$. *Phys. Rev. B* **2005**, *72*, No. 094303.

(52) Omata, T.; Noguchi, Y.; Otsuka-Yao-Matsuo, S. Infrared Study of High-Temperature Proton-Conducting Aliovalently Doped $SrZrO_3$ and $BaZrO_3$ Formation of YO_6 Clusters in Y-Doped $SrZrO_3$. *J. Electrochem. Soc.* **2005**, *156*, E200−E205.

(53) Ishiyama, T.; Kishimoto, H.; Develos-Bagarinao, K.; Yamaji, K.; Yamaguchi, T.; Fujishiro, Y. Dissociation behavior of protons incorporated in yttrium doped barium zirconate. *J. Solid State Chem.* **2017**, *252*, 22−27.

(54) Yamazoe, N.; Fuchigami, J.; Kishikawa, M.; Seiyama, T. Interactions of tin oxide surface with O2, H2O AND H2. *Surf. Sci.* **1979**, *86*, 335−344.

(55) Tang, W.; Ding, H.; Bian, W.; Regalado Vera, C. Y.; Gomez, J. Y.; Dong, Y.; Li, J.; Wu, W.; Fan, W.; Zhou, M.; et al. An Unbalanced Battle in Excellence: Revealing Effect of Ni/Co Occupancy on Water Splitting and Oxygen Reduction Reactions in Triple-Conducting Oxides for Protonic Ceramic Electrochemical Cells. *Small* **2022**, *18*, No. e2201953.

(56) Takahashi, H.; Oikawa, I.; Takamura, H. Atomistic Insight into the Correlation among Oxygen Vacancies, Protonic Defects, and the Acceptor Dopants in Sc-Doped $BaZrO_3$ Using First-Principles Calculations. *J. Phys. Chem. C* **2018**, *122*, 6501−6507.

(57) Noferini, D.; Koza, M. M.; Rahman, S. M. H.; Evenson, Z.; Nilsen, G. J.; Eriksson, S.; Wildes, A. R.; Karlsson, M. Role of the doping level in localized proton motions in acceptor-doped barium zirconate proton conductors. *Phys. Chem. Chem. Phys.* **2018**, *20*, 13697−13704.

(58) Draber, F. M.; Ader, C.; Arnold, J. P.; Eisele, S.; Grieshammer, S.; Yamaguchi, S.; Martin, M. Nanoscale percolation in doped $BaZrO_3$ for high proton mobility. *Nat. Mater.* **2020**, *19*, 338−346.

(59) Uedono, A.; Shimayama, K.; Kiyohara, M.; Chen, Z. Q.; Yamabe, K. Study of oxygen vacancies in $SrTiO_3$ by positron annihilation. *J. Appl. Phys.* **2002**, *92*, 2697−2702.

(60) Jiang, X.; Zhang, Y.; Jiang, J.; Rong, Y.; Wang, Y.; Wu, Y.; Pan, C. Characterization of Oxygen Vacancy Associates within Hydrogenated TiO_2: A Positron Annihilation Study. *J. Phys. Chem. C* **2012**, *116*, 22619−22624.

(61) Seeger, A. The Study of Defects in Crystals by Positron Annihilation. *Appl. Phys.* **1974**, *4*, 183−199.

(62) Campillo Robles, J. M.; Ogando, E.; Plazaola, F. Positron lifetime calculation for the elements of the periodic table. *J. Phys. Condens Matter.* **2007**, *19*, No. 176222.

(63) Mohsen, M.; Krause-Rehberg, R.; Massoud, A. M.; Langhammer, H. T. Donor-doping effect in BaTiO3 ceramics using positron annihilation spectroscopy. *Radiat. Phys. Chem.* **2003**, *68*, 549−552.

(64) Gorgol, M.; Zaleski, R.; Kierys, A.; Kamiński, D.; Strzałkowski, K.; Fedus, K. Positron lifetime spectroscopy of defect structures in Cd1−xZnxTe mixed crystals grown by vertical Bridgman−Stockbarger method. *Acta Crystallogr., Sect. B: Struct. Sci., Cryst. Eng. Mater.* **2021**, *77*, 515−525.

(65) Čížek, J.; Melikhova, O.; Procházka, I.; Kuriplach, J.; Kužel, R.; Brauer, G.; Anwand, W.; Konstantinova, T. E.; Danilenko, I. A. Defect studies of nanocrystalline zirconia powders and sintered ceramics. *Phys. Rev. B* **2010**, *81*, No. 024116.

(66) Han, D.; Goto, K.; Majima, M.; Uda, T. Proton Conductive $BaZr_{0.8-x}Ce_xY_{0.2}O_{3-\delta}$: Influence of NiO Sintering Additive on Crystal Structure, Hydration Behavior, and Conduction Properties. *ChemSusChem* **2021**, *14*, 614−623.

(67) Massoud, A. M.; Krause-Rehberg, R.; Langhammer, H. T.; Gebauer, J.; Mohsen, M. Defect Studies in BaTiO3 Ceramics Using Positron Annihilation Spectroscopy. *Mater. Sci. Forum* **2001**, *363−365*, 144−146.

(68) Bordulev, Y. S.; Lee, K.; Laptev, R. S.; Kudiiarov, V. N.; Lider, A. M. Positron Spectroscopy of Defects in Hydrogen-Saturated Zirconium. *Defect Diffus. Forum* **2017**, *373*, 138−141.

(69) Bjørheim, T. S.; Rahman, S. M.; Eriksson, S. G.; Knee, C. S.; Haugsrud, R. Hydration thermodynamics of the proton conducting oxygen-deficient perovskite series $BaTi_{1-x}M_xO_{3-x/2}$ with M = In or Sc. *Inorg. Chem.* **2015**, *54*, 2858−2865.

(70) Rowberg, A. J. E.; Weston, L.; Van de Walle, C. G. Optimizing Proton Conductivity in Zirconates through Defect Engineering. *ACS Appl. Energy Mater.* **2019**, *2*, 2611−2619.

(71) Toyoura, K.; Fujii, T.; Hatada, N.; Han, D.; Uda, T. Carrier−Carrier Interaction in Proton-Conducting Perovskites: Carrier Blocking vs Trap-Site Filling. *J. Phys. Chem. C* **2019**, *123*, 26823−26830.

Supporting Information

Improving Proton Conductivity by Navigating Proton Trapping in High Scandium Doped Barium Zirconate Electrolytes

Clarita Y. Regalado Vera [1,2], Hanping Ding [1,3,*], Jagoda Urban-Klaehn [1], Meng Li [1], Zeyu Zhao [1], Frederick Stewart [1], Hanchen Tian [4], Xingbo Liu [4], Yanhao Dong [5], Ju Li [6], Meng Zhou [2], Hongmei Luo [2,*], Dong Ding [1,*]

[1] Energy and Environment Science & Technology, Idaho National Laboratory, Idaho Falls, ID 83415, USA

[2] Department of Chemical and Materials Engineering, New Mexico State University, Las Cruces, NM 88003, USA

[3] School of Aerospace and Mechanical Engineering, University of Oklahoma, Norman, OK 73019, USA

[4] Department of Mechanical and Aerospace Engineering, West Virginia University, Morgantown, WV 26506, USA

[5] Department of Nuclear Science and Engineering, Massachusetts Institute of Technology, Cambridge, MA 02139, USA
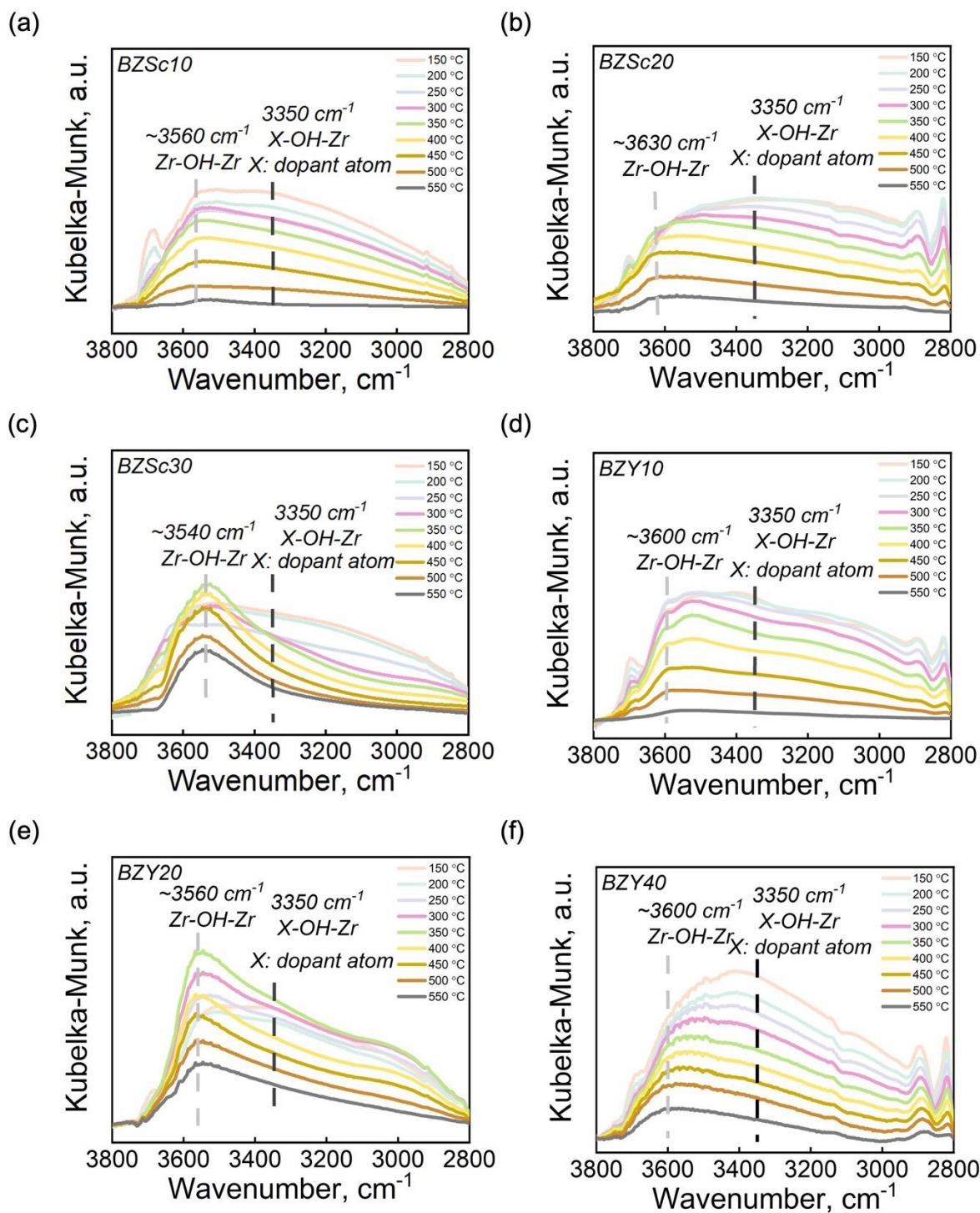
Figure S1. Diffuse reflectance Fourier transform spectroscopy spectra of (a) BZSc10, (b) BZSc20, (c) BZSc30, (d) BZY10, (e) BZY20 and (f) BZY40 during dehydration showing the bands assigned to Zr-OH-Zr and X-OH-Zr, X: dopant atom according to ref. [1].
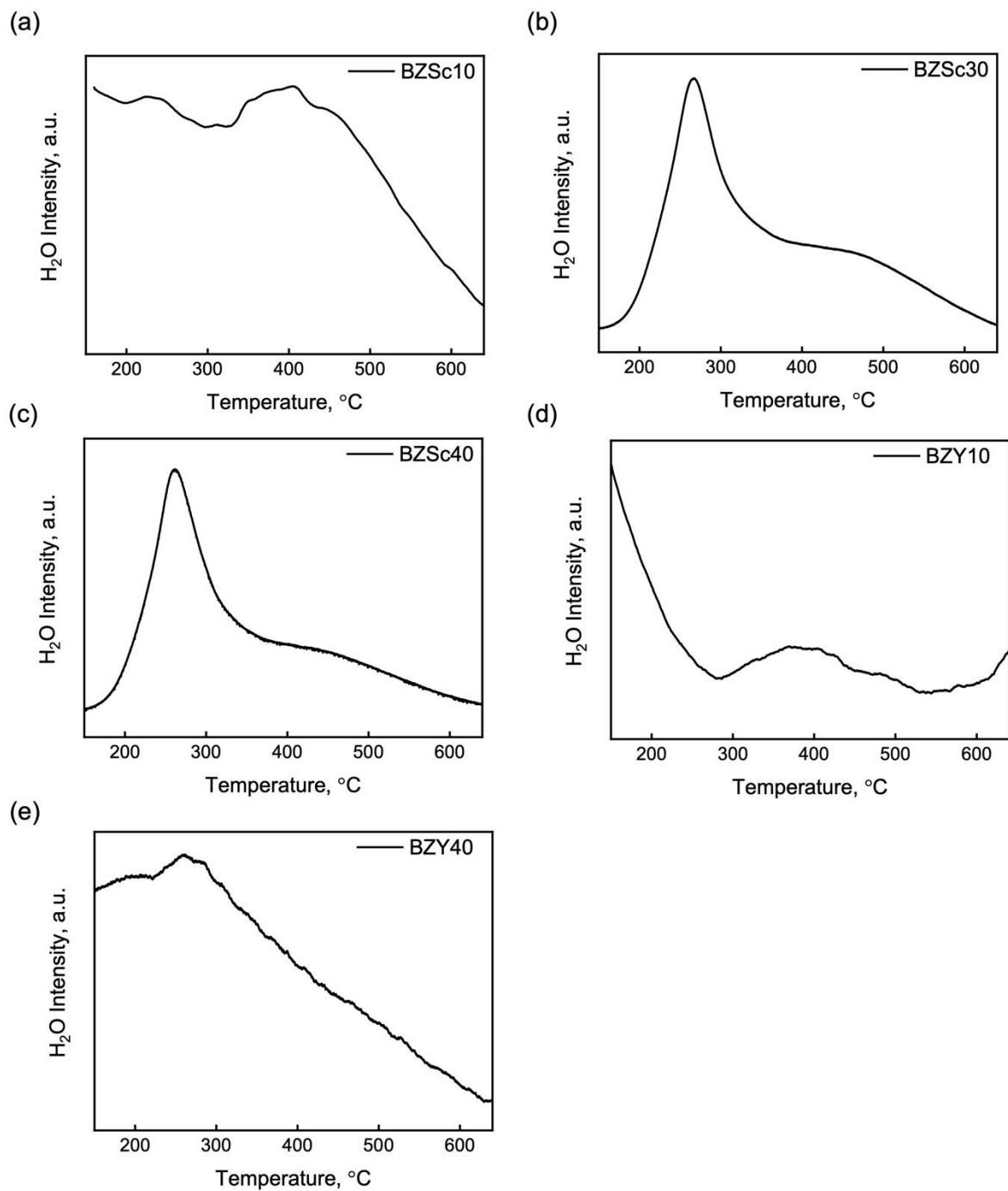
Figure S2. H_2O – temperature programmed desorption of (a) BZSc10, (b) BZSc30, (c) BZSc40, (d) BZY10, and (e) BZY40.
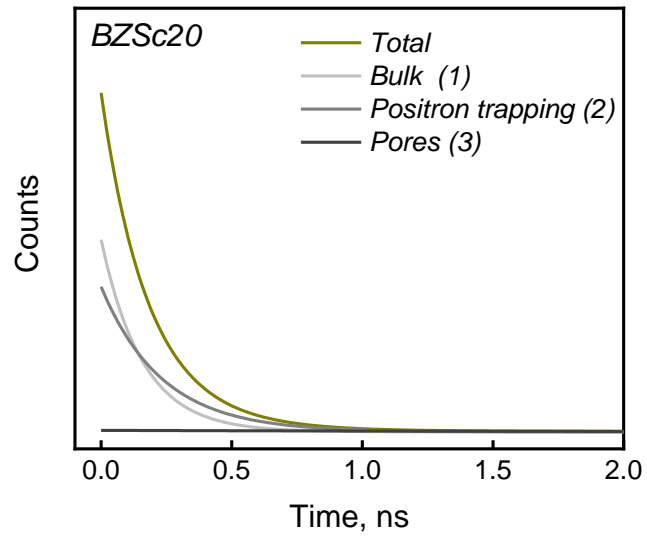
Figure S3. Positron annihilation lifetime spectroscopy response of BZSc20.
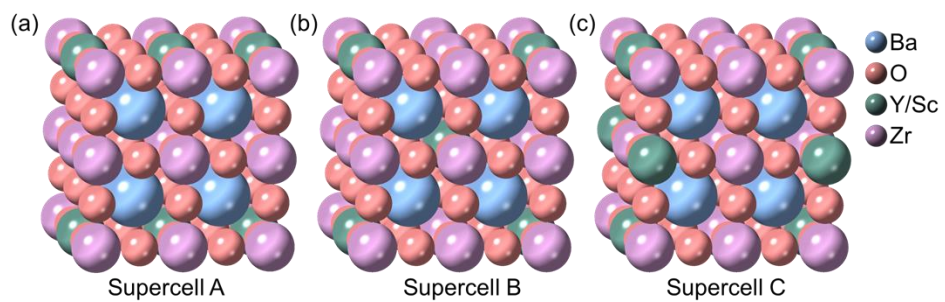
Figure S4. Supercell lattice of 25 mol. % Sc or Y-doped BaZrO$_3$ with possible distributions of dopants, designated as Supercell A, B, and C, respectively.
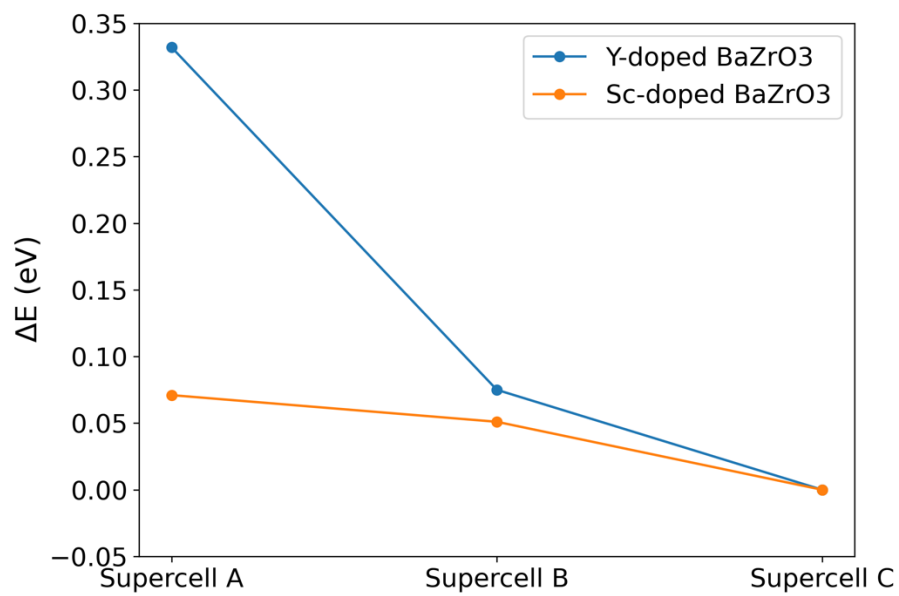
Figure S5. Relative energy differences (ΔE) for three supercells of Sc-doped $BaZrO_3$ and Y-doped $BaZrO_3$. The lattice configuration of supercell C turns out to be the most stable one in both cases.
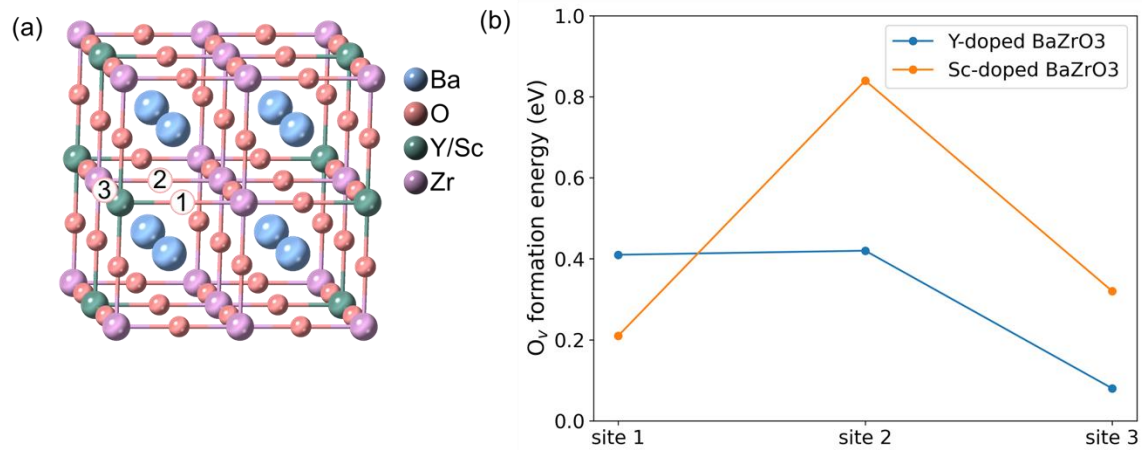
Figure S6. (a) Non-equivalent oxygen vacancy sites in Y/Sc-doped $BaZrO_3$ lattice, labeled as 1, 2, and 3. (b) The formation energies of oxygen vacancy (O_v) at different sites in Sc-doped $BaZrO_3$ and Y-doped $BaZrO_3$ lattice.
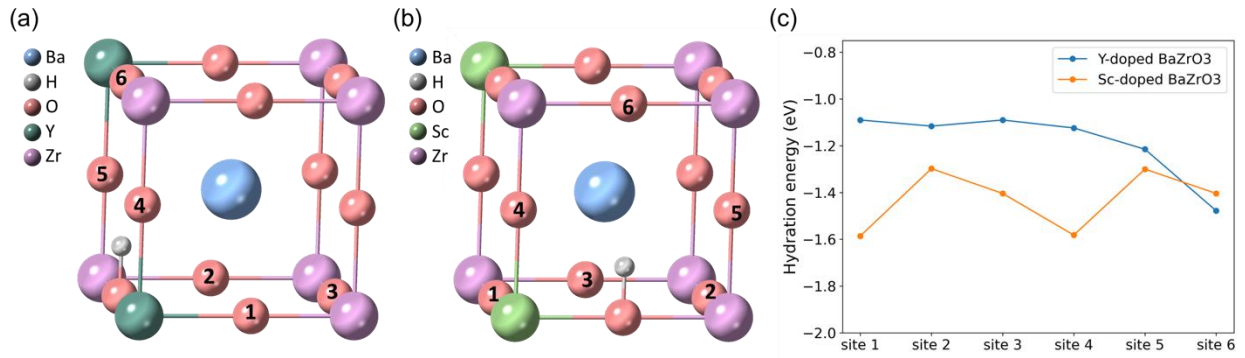
Figure S7. The hydration process with an OH occupies an oxygen vacancy site, and a proton bonded on a neighboring O site. Possible proton absorption sites in (a) Y-doped BaZrO$_3$ lattice and (b) Sc-doped BaZrO$_3$ lattice illustrated by a quarter of their supercells. (c) Hydration energies of the proton on different O sites.

Table S1. Enthalpy and entropy of hydration for Sc-doped $BaZrO_3$ and Y-doped $BaZrO_3$ materials.

Material	ΔH kJ/mol	ΔS J/mol K
$BaZr_{0.9}Sc_{0.1}O_{3-\delta}$	-91	-116
$BaZr_{0.8}Sc_{0.2}O_{3-\delta}$	-131	-144
$BaZr_{0.7}Sc_{0.3}O_{3-\delta}$	-111	-118
$BaZr_{0.6}Sc_{0.4}O_{3-\delta}$	-131	-140
$BaZr_{0.8}Y_{0.2}O_{3-\delta}$	-96	-126

Table S2. Lattice parameters and relative energies of Supercell A, B, C for 25 mol. % Y/Sc-doped $BaZrO_3$

Composition	Supercell type	a (Å)	b (Å)	c (Å)	α=β=γ (°)	Relative energy (eV)
25 mol. % Y doped $BaZrO_3$	A	8.559	8.580	8.583	90	0.33
	B	8.578	8.578	8.584	90	0.08
	C	8.582	8.585	8.582	90	0
25 mol. % Sc doped $BaZrO_3$	A	8.462	8.466	8.469	90	0.07
	B	8.464	8.464	8.469	90	0.05
	C	8.467	8.471	8.467	90	0

References

(1) Karlsson, M.; Björketun, M. E.; Sundell, P. G.; Matic, A.; Wahnström, G.; Engberg, D.; Börjesson, L.; Ahmed, I.; Eriksson, S.; Berastegui, P. Vibrational properties of protons in hydrated $BaIn_xZr_{1-x}O_{3-x/2}$. *Physical Review B* **2005**, *72* (9). DOI: 10.1103/PhysRevB.72.094303.